

Phonon-mediated dimensional crossover in bilayer CrI_3

M. Rodriguez-Vega,^{1,2,*} Ze-Xun Lin,^{1,2,*} A. Leonardo,^{3,4} A. Ernst,^{5,6}
G. Chaudhary,⁷ M. G. Vergniory,^{3,8} and Gregory A. Fiete^{2,1,9}

¹*Department of Physics, The University of Texas at Austin, Austin, TX 78712, USA*

²*Department of Physics, Northeastern University, Boston, MA 02115, USA*

³*Donostia International Physics Center, San Sebastian, Spain*

⁴*Applied Physics Department II, University of the Basque Country UPV/EHU, Bilbao, Spain.*

⁵*Institut für Theoretische Physik, Johannes Kepler Universität, A 4040 Linz, Austria*

⁶*Max-Planck-Institut für Mikrostrukturphysik, Weinberg 2, D-06120 Halle, Germany*

⁷*James Franck Institute, Department of Physics, The University of Chicago, Chicago, IL 60637*

⁸*IKERBASQUE, Basque Foundation for Science, Bilbao, Spain*

⁹*Department of Physics, Massachusetts Institute of Technology, Cambridge, MA 02139, USA*

(Dated: May 23, 2022)

In bilayer CrI_3 , experimental and theoretical studies suggest that the magnetic order is closely related to the layer stacking configuration. In this work, we study the effect of dynamical lattice distortions, induced by non-linear phonon coupling, in the magnetic order of the bilayer system. We use density functional theory to determine the phonon properties and group theory to obtain the allowed phonon-phonon interactions. We find that the bilayer structure possesses low-frequency Raman modes that can be non-linearly activated upon the coherent photo-excitation of a suitable infrared phonon mode. This transient lattice modification in turn inverts the sign of the interlayer spin interaction for parameters accessible in experiments, indicating a low-frequency light-induced antiferromagnet-to-ferromagnet transition.

The control of ordered states of matter such as magnetism, superconductivity or charge and spin density waves is one of the more sought after effects in the field. In equilibrium, this can be achieved by turning the knobs provided by temperature, strain, pressure, or chemical composition. However, the nature of these methods limits the possibility to integrate the materials into devices for technological applications due undesirably slow control and non-reversibility. In recent years, a new approach has emerged which allows *in-situ* manipulation: driving systems out of equilibrium by irradiating them with light [1–30]. Recent experiments have demonstrated the existence of Floquet states in topological insulators [31, 32], the possibility to transiently enhance superconductivity [33–35], the existence of light-induced anomalous Hall states in graphene [36], light-induced metastable charge-density-wave states in 1T-TaS_2 [37], optical pulse-induced metastable metallic phases hidden in charge ordered insulating phases [38, 39], and metastable ferroelectric phases in titanates [40].

Finding suitable platforms to realize non-equilibrium transitions represents the first main challenge. Recently, interest in the van der Waals bulk ferromagnet chromium triiodide (CrI_3) [41, 42] has been renewed with the discovery that it is stable in its monolayer form, where the chromium atoms arrange in a hexagonal lattice and the iodine atoms order on a side-sharing octahedral cage around each chromium atom as shown in Fig. 1(a-b). Monolayer CrI_3 presents out-of-plane magnetization stabilized by anisotropies [43] and a Curie temperature $T \sim 45$ K [44]. The origin of the anisotropies is still a subject of intense theoretical and experimental investigations [45–47].

In bulk form, CrI_3 exhibits a structural phase transition near $T = 210 - 220$ K. This structural transition is accompanied by an anomaly in the magnetic susceptibility, but no magnetic ordering [42]. At $T = 61$ K, CrI_3 exhibits a transition from paramagnet to ferromagnet [42], with an easy-axis perpendicular to the 2D planes. There is evidence that suggests CrI_3 is a Mott insulator with a band gap close to 1.2 eV [41, 42]. Recent experiments have measured very large tunneling magnetoresistance [48, 49], suggesting potential applications in spintronics devices.

Experiments have determined that bilayer CrI_3 (b- CrI_3) presents an antiferromagnetic (AFM) ground-state [44, 49–52], with monoclinic crystal structure (see Fig. 1(c-d)). Single-spin microscopy [53] and polarization resolved Raman spectroscopy [54] measurements have established a strong connection between the magnetic order and the stacking configuration in few-layers CrI_3 . Furthermore, it has been shown that the magnetic order can be controlled in equilibrium by doping [55] and applying pressure [56] in b- CrI_3 samples. These experimental results have been followed by theoretical studies investigating the origin of the AFM order and its link to the lattice configuration [57–59] and the mechanism behind the AFM-FM transition in doped b- CrI_3 [60].

In this Letter, we leverage these theoretical and experimental results, and consider the possibility to dynamically tune the magnetic order in b- CrI_3 using low-frequency light to coherently drive suitable phonon modes. We start with a group theory analysis to determine the feasibility of the non-linear phonon process required. Guided by these results, we perform first principles calculations to find phonon frequencies, eigenmodes

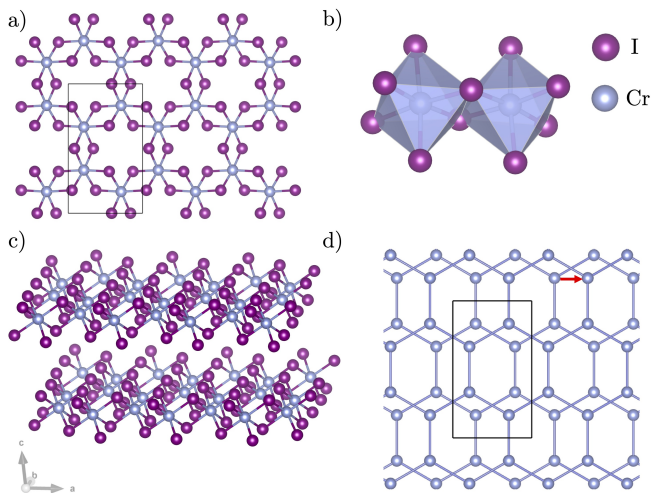


FIG. 1. (Color online) a) Monolayer CrI_3 lattice structure. The conventional unit cell is shown with solid lines. b) Cr^{+3} atoms surrounded by an edge-sharing I octahedral cage. c) b- CrI_3 crystal structure with space group $C2/m$ associated AFM ground state. The top layer is shifted with respect to the bottom layer by $[1/3 \ 0 \ 0]$. d) Top view with I atoms suppressed for clarity. The red arrow indicates the relative shift. The black box indicates the conventional unit cell, and the I atoms were suppressed for clarity. The lattice structures were created with VESTA [61].

and non-linear phonon coupling strengths. We then analyze the equations of motion for the driven phonons and their impact on the lattice structure. Finally, we determine the effect of such transient lattice deformations in the magnetic order and find the possibility to induce a sign change in the interlayer exchange interaction using experimentally-accessible parameters.

Group theory analysis. Recent first-principles studies indicate that there is a direct relation between the magnetic ground state and the relative stacking order between the layers [57, 59, 62]. The FM phase presents an AB stacking with space group $R\bar{3}$ (point group S_6), while the AFM ground state is accompanied by an AB' stacking with space group $C2/m$ and point group C_{2h} . In Fig. 1(d), we show the AB' stacking configuration (omitting the I atoms for clarity), which corresponds to an AA stacking shifted by $1/3$ in lattice vector units. In bulk CrI_3 , the high-temperature phase belongs to the space group $C2/m$, while the low temperature phase to the space group $R\bar{3}$. Both structures are related by a relative shift of the layers leaving each individual layer unaltered. Since experiments find an AFM order in the ground state [44], in our analysis we assume the configuration corresponding to the C_{2h} space group. The conventional unit cell is indicated by the solid black lines in Fig. 1(d), which contains 8 Cr atoms and 24 I atoms. For our calculations, we work with the primitive unit cell, which contains $N = 16$ atoms. The unit cell trans-

formation, and the C_{2h} point group character table are listed in the Supplemental Material [63]. The total number of phonon modes is then $3N = 48$. We have 3 acoustic modes and $3N - 3 = 45$ optical modes. We obtain that the equivalence representation is given by $\Gamma^{equiv} = 5A_g \oplus 3B_g \oplus 3A_u \oplus 5B_u$. In the C_{2h} point group, the representation of the vector is $\Gamma_{vec} = 2A_u \oplus B_u$, which leads to the lattice vibration representation $\Gamma_{latt.vib.} = \Gamma^{equiv} \otimes \Gamma_{vec} = 13A_g \oplus 11B_g \oplus 11A_u \oplus 13B_u$. From the symmetry of the generating functions (see the character table in the Supplemental Material [63]), 24 modes are Raman active (13 with totally symmetric A_g representation and 11 with B_g representation) and 24 infrared active modes [64].

As we have discussed, based on DFT studies [57, 58], the magnetic ground state is correlated with the relative position of the stacked layers. Therefore, we posit that a Raman mode involving a relative shift between the layers might influence the magnetic order. In order to test if such a mode is allowed by symmetry, we construct the projection operators [65, 66] $\hat{P}_{kl}^{(\Gamma_n)} = \frac{l_n}{h} \sum_{C_\alpha} \left(D_{kl}^{(\Gamma_n)}(C_\alpha) \right)^* \hat{P}(C_\alpha)$, where Γ_n are the irreducible representations, C_α are the elements of the group, $D_{kl}^{(\Gamma_n)}(C_\alpha)$ is the irreducible matrix representation of element C_α , h is the order of the group, and l_n is the dimension of the irreducible representation. Finally, $\hat{P}(C_\alpha)$ are $3N \times 3N$ matrices that form the displacement representation. Applying the projection operators \hat{P}^{A_g} and \hat{P}^{B_g} to random displacements of the atoms, we find that modes with one layer uniformly displaced in the $[1 \ 1 \ 0]$ direction, while the other in the $[\bar{1} \ \bar{1} \ 0]$ direction is allowed by symmetry and belong to the totally-symmetric A_g representation (Fig. 2(c)). Similarly, modes where one layer is displaced in the $[0 \ 0 \ 1]$ direction and the other one in the $[0 \ 0 \ \bar{1}]$ belongs to the A_g representation (see Fig. 2(b)). On the other hand, layer displacements in the directions $[\bar{1} \ 1 \ 0]$ and $[1 \ \bar{1} \ 0]$, belong to the B_g representation (see Fig. 2(d)). We will show that these Raman modes can be effectively manipulated via indirect coupling with light to control the magnetic order.

Phonon frequencies. Once we determine that these modes are allowed by symmetry, we calculate the phonon frequencies using density functional perturbation theory (DFPT) and finite difference methods as implemented in QUANTUM ESPRESSO [67, 68] and VASP [69, 70], respectively. We find excellent agreement among all the approaches considered. The details of the calculations are shown in the Supplemental Material [63]. In Fig. 2(a), we plot the full set of frequencies of the Γ -point phonons.

We find that the three low-frequency modes (apart from the three omitted zero-frequency acoustic modes) are Raman active, and correspond to relative displacement between the layers in different directions, in agreement with the group theory results. The lowest-frequency mode, $\Omega = 0.460$ THz, belongs to the A_g

representation, and the real-space displacement is shown in Fig. 2(c). The next phonon mode is very close in frequency, $\Omega = 0.467$ THz, however, it belongs to the B_g representation (Fig. 2(d)). The mode with frequency $\Omega = 0.959$ THz belongs to the A_g representation and corresponds to a relative displacement perpendicular to the layers, as shown in Fig. 2(b).

Non-linear phonon processes have been proposed for transient modification of the symmetries of the system, which can be accompanied by changes in the ground-state properties [3, 4, 7–9, 12–15]. Now, we derive the non-linear phonon potential resulting from coupling between infrared (Q_{IR}) and Raman (Q_{R}) active modes in b-CrI₃. In an invariant polynomial under the operations of a given group, coupling between two modes is allowed only if it contains the totally symmetric representation [65, 66]. We consider the coherent light-induced excitation of a non-degenerate infrared active mode with representation B_u . In principle, this IR mode is allowed to couple non-linearly to all A_g and B_g Raman modes in the C_{2h} point group. However, the low frequency of the soft modes involving relative motion between the layers, compared with the rest of the Raman phonon modes allows us to focus on this modes, as we will show. Up to cubic order, the non-linear potential functional including the three low-frequency phonon modes is given by

$$\begin{aligned}
 V[Q_{\text{IR}}, Q_{\text{R}(i)}] &= \frac{1}{2}\Omega_{\text{IR}}^2 Q_{\text{IR}}^2 + \sum_{i=1}^2 \frac{1}{2}\Omega_{\text{R}(i)}^2 Q_{\text{R}(i)}^2 \\
 &+ \sum_{i=1}^2 \frac{\beta_i}{3} Q_{\text{R}(i)}^3 + Q_{\text{IR}}^2 \sum_{i=1}^2 \gamma_i Q_{\text{R}(i)} + \delta Q_{\text{R}(1)}^2 Q_{\text{R}(2)} \\
 &+ \epsilon Q_{\text{R}(1)} Q_{\text{R}(2)}^2 + Q_{\text{R}(3)}^2 \sum_{i=1}^2 \zeta_i Q_{\text{R}(i)}. \quad (1)
 \end{aligned}$$

The numerical value of the coefficients is obtained using first-principles calculations. In the Supplemental Material [63] we outline the procedure we used following Ref. [4], we plot the energy surfaces obtained by varying the corresponding phonon mode amplitudes, and display the numerical values of the coefficients obtained by fitting Eq. (1).

Under an external drive with frequency Ω , the potential acquires the time-dependent term [71, 72] $V_D[Q_{\text{IR}}] = \mathbf{Z}^* \cdot \mathbf{E}_0 \sin(\Omega t) F(t) Q_{\text{IR}}$, where \mathbf{E}_0 is the electric field amplitude, and \mathbf{Z}^* is the mode effective charge vector [71, 73]. $F(t) = \exp\{-t^2/(2\tau^2)\}$ is the Gaussian laser profile, with variance τ^2 . Assuming that damping can be neglected, the general differential equations governing the dynamics of one infrared mode coupled to m Raman modes are obtained from the relations $\partial_t^2 Q_{\text{R}(i)} = -\partial_{Q_{\text{R}(i)}} V[Q_{\text{IR}}, Q_{\text{R}(i)}]$, and $\partial_t^2 Q_{\text{IR}} = -\partial_{Q_{\text{IR}}} V[Q_{\text{IR}}, Q_{\text{R}(i)}]$, which correspond to a set of $m + 1$ coupled differential equations that we solve numerically in the general case. The in-

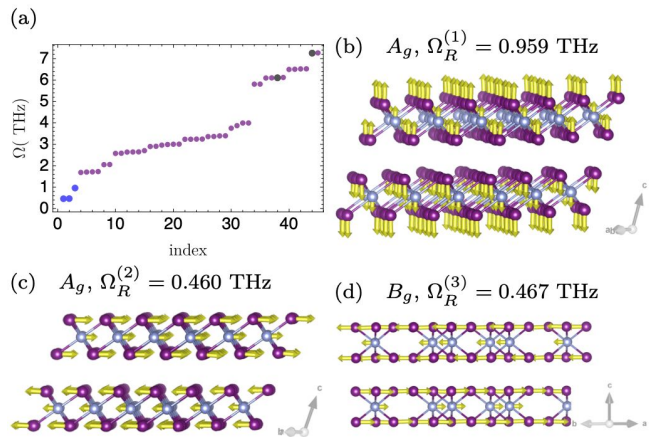


FIG. 2. (Color online) (a) b-CrI₃ phonon frequencies in the space group $C2/m$ and AFM ground state. The low-frequency blue dots correspond Raman modes involving layer relative shifts. The gray dots correspond to IR modes that directly couple to the light. The acoustic modes are not shown. (b-d) b-CrI₃ (space group $C2/m$ and AFM ground state) phonon displacements relevant for the non-linear dynamics.

dex $i = 1, \dots, m$ runs over the Raman modes. In the absence of coupling with the Raman modes, the IR mode dynamics are described by $\partial_t^2 Q_{\text{IR}} = -\Omega_{\text{IR}}^2 Q_{\text{IR}} - Z^* E_0 \sin(\Omega t) F(t)$. In the resonant case $\Omega = \Omega_{\text{IR}}$, and impulsive limit $\Omega_{\text{IR}} \tau \ll 1$, we find $Q_{\text{IR}}(t) = \sqrt{2\pi} Z^* E_0 \tau / \Omega_{\text{IR}} \cos(\Omega_{\text{IR}} t) \sinh[(\Omega_{\text{IR}} \tau)^2] e^{-(\Omega_{\text{IR}} \tau)^2}$ where the boundary conditions are $Q_{\text{IR}}(-\infty) = \partial_t Q_{\text{IR}}(-\infty) = 0$ [4]. The amplitude of the excited IR modes scales linearly with the electric field and the mode effective charge.

Now we add coupling with one A_g Raman mode. The potential in Eq. (1) simplifies to $V[Q_{\text{IR}}, Q_{\text{R}}] = \frac{1}{2}\Omega_{\text{IR}}^2 Q_{\text{IR}}^2 + \frac{1}{2}\Omega_{\text{R}}^2 Q_{\text{R}}^2 + \gamma Q_{\text{IR}}^2 Q_{\text{R}}$. The cubic term γ is responsible for the *ionic Raman scattering* (IRS) [72, 74]. Within this mechanism, the infrared active mode is used to drive Raman scattering processes through anharmonic terms in the potential, and leads coherent oscillations around a new displaced equilibrium position. Theoretical works have also proposed this cubic non-linear coupling mechanism to tune magnetic order in RTiO₃ [16, 17], investigate light-induced dynamical symmetry breaking [4], modulate the structure of YBa₂Cu₃O and related effects in the magnetic order [18]. On the experimental side, the response of YBa₂Cu₃O_{6+x} to optical pulses has been investigated [75], and experimental detection of possible light-induced superconductivity has been reported [35].

From the equilibrium condition $\partial_{Q_{\text{R}}} V[Q_{\text{IR}}, Q_{\text{R}}] = 0$, we find that the potential is minimized when [7] $Q_{\text{R}} = -\gamma Q_{\text{IR}}^2 / \Omega_{\text{R}}^2$. Therefore, we obtain larger displaced equilibrium positions effects for low-frequency Raman modes. This argument allows us to limit our discussion to the three low-frequency Raman modes shown in Fig. 2(b-d).

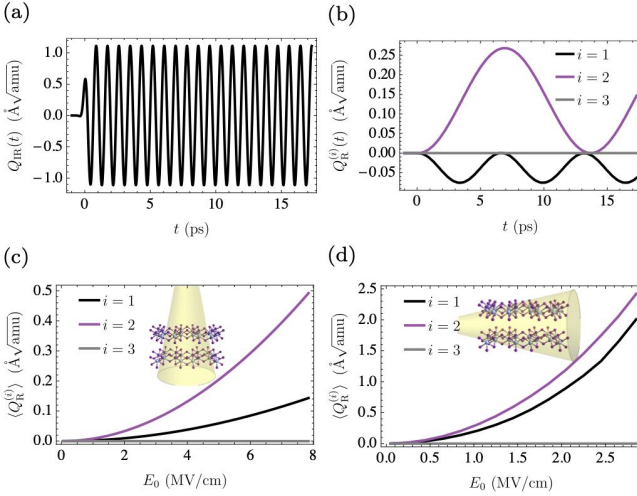


FIG. 3. (Color online) (a) Infrared Q_{IR} and (b) Raman modes $Q_R^{(i)}$, for $i = 1, 2, 3$ oscillations as a function of time for b-CrI₃ for a laser incident in the z -direction. The drive parameters used are $E = 4$ MV/cm, $\tau = 0.2$ ps. (c) and (d) Average displacement for the Raman modes $Q_R^{(i)}$ non-linearly coupled to the excited infrared mode Q_{IR} , as shown in the insets. The drive parameter used is $\tau = 0.2$ ps.

Considering the cubic term as a perturbation, we find the time-dependence of the Raman mode is given by

$$Q_R(t) = \frac{\gamma\pi(Z^*E_0\tau^3)^2}{(4\Omega_{IR}^2 - \Omega_R^2)} \frac{\Omega_{IR}^2}{\Omega_R^2} (\Omega_R^2 \cos(2\Omega_{IR}t) + 2(\Omega_{IR}^2 - \Omega_R^2) \cos(\Omega_R t) + \Omega_R^2 - 4\Omega_{IR}^2). \quad (2)$$

In the resonant limit $\Omega_R = 2\Omega_{IR}$, the solution is given by $Q_R(t) = -\gamma\pi(Z^*E_0\tau^3)^2 \sin(\Omega_{IR}t) (\sin(\Omega_{IR}t) + \Omega_{IR}t \cos(\Omega_{IR}t)) / 2$.

Additional constraints for the IR mode selection arise from current experimental capabilities for strong THz pulse generation. Strong fields of up to 100 MV cm⁻¹ have been achieved in the literature in the range 15 – 50 THz [76, 77].

Now we investigate the non-linear dynamics of the three Raman phonon modes of interest. We consider laser pulses incident along the z and y -directions, as shown in the insets of Fig. 3(c) and (d). The IR mode with frequency $\Omega_{IR} = 7.19$ THz (see Fig. 2(a), top grey dot) is parallel to the z -direction with a Born effective charge Z^* four times larger than any other IR mode parallel to the z -direction with lower frequency. On the other hand, the IR mode with frequency $\Omega_{IR} = 6.104$ THz is parallel to the y -direction with a Born effective charge approximately two order of magnitude larger than any other mode with non-zero overlapping with the laser incident in the y -direction. Therefore, considering only one IR mode is justified in our case.

The numerical solutions for Q_{IR} and $Q_R^{(i)}$ are shown in Fig. 3(a-b) for an experimentally accessible elec-

tric field $E_0 = 4$ MV/cm, with $\tau = 0.2$ ps incident in the z -direction. The totally symmetric mode c ($\Omega_R^{(2)} = 0.46$ THz) shows the largest amplitude, followed by the mode $Q_R^{(1)}$ ($\Omega_R^{(1)} = 0.959$ THz) which involves displacements in the \hat{z} -direction, perpendicular to the layers. The Raman mode $Q_R^{(3)}$ with B_g representation does not participate in the dynamics due to the weak coupling with $Q_R^{(1)}$ and $Q_R^{(2)}$ modes, and the absence of non-linear coupling with the infrared mode Q_{IR} up to cubic order. In Fig. 3(c) ((d)), we plot the averaged displacements as a function of electric field amplitude for a laser incident in the z -direction (y -direction). Assuming an electric field amplitude $E_0 = 3.5$ MV/cm incident in the y -direction, we obtain $\langle Q_R^{(2)} \rangle = 4.8 \text{ \AA}/\sqrt{\text{amu}}$, which corresponds to a real-space displacement of 2.26% of the in-plane lattice parameter $a = b = 6.85 \text{ \AA}$. Next, we will show that the relative displacements accessible using non-linear phonon processes are large enough to induce a change in the exchange interactions.

Effective spin interaction. Recently, a combined study employing group theory and ferromagnetic resonance measurements [46] proposed that CrI₃ is described by the Heisenberg-Kitaev Hamiltonian $\mathcal{H} = \mathcal{H}_{\text{intra}} + \mathcal{H}_{\text{inter}}$, where the intralayer sector is given by [78, 79]

$$\mathcal{H}_{\text{intra}} = \sum_{\langle ij \rangle \in \lambda\mu(\nu)} J_{ij} \mathbf{s}_i \cdot \mathbf{s}_j + K s_i^\nu s_j^\nu + \Gamma (s_i^\lambda s_j^\mu + s_i^\mu s_j^\lambda),$$

where the first term corresponds to the isotropic Heisenberg interaction, the second term is the Kitaev interaction, which introduces a bond-dependent anisotropy [78], and the Γ term corresponds to off-diagonal exchange [79]. In Ref. [46], the intra-layer interaction constants for bulk CrI₃ were determined experimentally to be $J = -0.2$ meV, $K = -5.2$ meV, and $\Gamma = -67.5 \mu\text{eV}$. The Heisenberg-Kitaev Hamiltonian $\mathcal{H}_{\text{intra}}$ has been extensively studied. The phase diagram has been determined [79], the spin-wave spectrum has been shown to carry nontrivial Chern numbers [80], and the magnon contribution to thermal conductivity has been determined [81]. The interlayer Hamiltonian has been assumed dominated by nearest-neighbor Heisenberg interactions, $\mathcal{H}_{\text{inter}} = \sum_{\langle ij \rangle \in \text{int.}} J_\perp \mathbf{s}_i \cdot \mathbf{s}_j$, with $J_\perp = 0.03$ meV in Ref. [46], and $J_\perp = 0.59$ meV in Ref. [45], as extracted from ferromagnetic resonance and inelastic neutron scattering measurements in bulk CrI₃, respectively. Although both experiments propose different intralayer spin models, both find that the interlayer energy scale is much smaller than the intralayer scales. We map the interlayer Hamiltonian into a Heisenberg model of the form $\mathcal{H}_{\text{inter}} = \frac{1}{2} \sum_{ij \in \text{int.}} J_{ij} \mathbf{s}_i \cdot \mathbf{s}_j$, and determine J_{ij} from first principles (generalized gradient approximation with Hubbard $U=1$ eV fixed to reproduce the b-CrI₃ critical temperature $T_C = 45$ K) using a Green's function approach and the magnetic force theorem (for a detailed explanation of the method, see Ref. [82]).

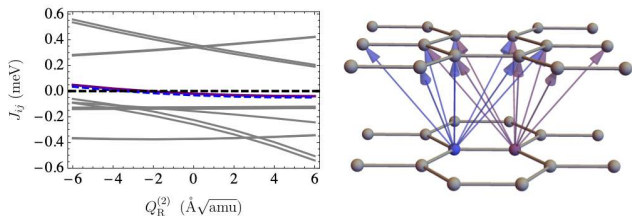


FIG. 4. (Color online) Interlayer exchange interactions as a function of Raman displacement $Q_R^{(2)}$. In the b-CrI₃ sketch, we indicate the relevant exchange interactions J_{ij} , where i and j correspond to magnetic moments in opposite layers. The highlighted purple and blue curves cross the zero (dashed) line and thus the preferred magnetization switches from AFM to FM.

The coupling between the spin and the phonons enters through the interatomic distance dependence of the exchange constants [83]. Under a lattice deformation, and for small deviations from the equilibrium position, the exchange interaction is given by

$$J[\mathbf{u}(t)] = J^0 + \delta J \hat{\delta} \cdot \mathbf{u}(t) + \mathcal{O}(\mathbf{u}(t)^2), \quad (3)$$

where J^0 corresponds to the equilibrium interaction, δJ is the strength of the first-order correction in the direction $\hat{\delta}$, and $\mathbf{u}(t)$ is the real-space phonon displacement. Given that the infrared phonon frequencies we propose to use ($\Omega_{\text{IR}} \approx 7.19, 6.1$ THz) are much larger than the relevant spin interactions ($\lesssim 1$ meV), to leading order, Floquet theory indicates that the effective interlayer exchange interaction becomes $J^{\text{eff}} = J^0 + \delta J \hat{\delta} \cdot \langle \mathbf{u}_R \rangle$, where $\langle \mathbf{u}_R \rangle$ is the time-averaged Raman mode displacement.

Therefore, in order to determine the effect of the non-linear phonon displacements, we compute the effective exchange interactions in b-CrI₃ for layers displaced with respect to each other in the direction of the $Q_R^{(2)}$ phonon. The obtained interlayer exchange interactions J_{ij} as a function of the Raman displacement amplitude are shown in Fig 4, revealing the complexity of the interlayer magnetic order in b-CrI₃. For $Q_R^{(2)} \approx 4 \text{ \AA}\sqrt{\text{amu}}$, within reach of the displacement amplitude induced by laser irradiation, two of the interlayer exchange interactions changes sign. Therefore, non-linear phononics offers a viable scheme to tune the exchange interactions in strongly correlated systems such as b-CrI₃.

Conclusions. In this work, we studied b-CrI₃ driven with low-frequency light pulses. We found that coherently driving an infrared mode can activate Raman modes involving relative displacements between the layers, which oscillate around new shifted equilibrium positions. The transient lattice distortions affect the exchange interactions and can lead to a change in sign in the interlayer interaction for a range of parameters accessible in experimental setups and allows the opportunity to change the magnetic order in a system via a drive

with minimal heating effects. Similar results should be possible for other layer materials with weak inter-layer bonds.

Acknowledgments. We thank Matthias Geilhufe for useful discussions on group theory and the use of GT-Pack, and D. M. Juraschek for useful discussions on non-linear phononics. This research was primarily supported by the National Science Foundation through the Center for Dynamics and Control of Materials: an NSF MRSEC under Cooperative Agreement No. DMR-1720595 and NSF Grant No. DMR-1949701. M.R-V thanks the hospitality of Aspen Center for Physics, supported by National Science Foundation grant PHY-1607611, where parts of this work were performed.

* These two authors contributed equally

- [1] T. Oka and H. Aoki, Phys. Rev. B **79**, 081406 (2009).
- [2] N. H. Lindner, G. Refael, and V. Galitski, Nat Phys **7**, 490 (2011).
- [3] M. Frst, R. Mankowsky, H. Bromberger, D. Fritz, H. Lemke, D. Zhu, M. Chollet, Y. Tomioka, Y. Tokura, R. Merlin, J. Hill, S. Johnson, and A. Cavalleri, Solid State Communications **169**, 24 (2013).
- [4] A. Subedi, A. Cavalleri, and A. Georges, Phys. Rev. B **89**, 220301 (2014).
- [5] J. H. Mentink, K. Balzer, and M. Eckstein, Nature Communications **6**, 6708 (2015).
- [6] M. Gu and J. M. Rondinelli, Phys. Rev. B **95**, 024109 (2017).
- [7] D. M. Juraschek, M. Fechner, and N. A. Spaldin, Phys. Rev. Lett. **118**, 054101 (2017).
- [8] D. M. Juraschek, M. Fechner, A. V. Balatsky, and N. A. Spaldin, Phys. Rev. Materials **1**, 014401 (2017).
- [9] A. Subedi, Phys. Rev. B **95**, 134113 (2017).
- [10] M. Babadi, M. Knap, I. Martin, G. Refael, and E. Demler, Phys. Rev. B **96**, 014512 (2017).
- [11] J. Liu, K. Hejazi, and L. Balents, Phys. Rev. Lett. **121**, 107201 (2018).
- [12] D. M. Juraschek and S. F. Maehrlein, Phys. Rev. B **97**, 174302 (2018).
- [13] D. M. Juraschek and N. A. Spaldin, Phys. Rev. Materials **3**, 064405 (2019).
- [14] D. M. Juraschek, Q. N. Meier, and P. Narang, Phys. Rev. Lett. **124**, 117401 (2020).
- [15] D. M. Juraschek, P. Narang, and N. A. Spaldin, "Phonon-magnetic analogs to opto-magnetic effects," (2019), arXiv:1912.00129 [cond-mat.mtrl-sci].
- [16] G. Khalsa and N. A. Benedek, npj Quantum Materials **3**, 15 (2018).
- [17] M. Gu and J. M. Rondinelli, Phys. Rev. B **98**, 024102 (2018).
- [18] M. Fechner and N. A. Spaldin, Phys. Rev. B **94**, 134307 (2016).
- [19] K. Hejazi, J. Liu, and L. Balents, Phys. Rev. B **99**, 205111 (2019).
- [20] M. A. Sentef, A. F. Kemper, A. Georges, and C. Kollath, Phys. Rev. B **93**, 144506 (2016).
- [21] M. A. Sentef, Phys. Rev. B **95**, 205111 (2017).

- [22] N. Tancogne-Dejean, M. A. Sentef, and A. Rubio, *Phys. Rev. Lett.* **121**, 097402 (2018).
- [23] S. Chaudhary, A. Haim, Y. Peng, and G. Refael, “Phonon-induced floquet second-order topological phases protected by space-time symmetries,” (2019), arXiv:1911.07892 [cond-mat.mes-hall].
- [24] S. Chaudhary, D. Hsieh, and G. Refael, *Phys. Rev. B* **100**, 220403 (2019).
- [25] M. Vogl, M. Rodriguez-Vega, and G. A. Fiete, “Effective floquet hamiltonians for periodically-driven twisted bilayer graphene,” (2020), arXiv:2002.05124 [cond-mat.mes-hall].
- [26] M. Vogl, M. Rodriguez-Vega, and G. A. Fiete, “Floquet engineering of interlayer couplings: Tuning the magic angle of twisted bilayer graphene at the exit of a waveguide,” (2020), arXiv:2001.04416 [cond-mat.mes-hall].
- [27] M. Vogl, P. Laurell, A. D. Barr, and G. A. Fiete, *Phys. Rev. X* **9**, 021037 (2019).
- [28] E. Baldini, C. A. Belvin, M. Rodriguez-Vega, I. O. Ozel, D. Legut, A. Kozłowski, A. M. Oleś, K. Parlinski, P. Piekarczyk, J. Lorenzana, G. A. Fiete, and N. Gedik, *Nature Physics* (2020).
- [29] Z. Gu, H. A. Fertig, D. P. Arovas, and A. Auerbach, *Phys. Rev. Lett.* **107**, 216601 (2011).
- [30] A. Kundu, H. A. Fertig, and B. Seradjeh, *Phys. Rev. Lett.* **116**, 016802 (2016).
- [31] Y. H. Wang, H. Steinberg, P. Jarillo-Herrero, and N. Gedik, *Science* **342**, 453 (2013).
- [32] F. Mahmood, C.-K. Chan, Z. Alpichshev, D. Gardner, Y. Lee, P. A. Lee, and N. Gedik, *Nature Physics* **12**, 306 (2016).
- [33] D. Fausti, R. I. Tobey, N. Dean, S. Kaiser, A. Dienst, M. C. Hoffmann, S. Pyon, T. Takayama, H. Takagi, and A. Cavalleri, *Science* **331**, 189 (2011).
- [34] R. Mankowsky, A. Subedi, M. Först, S. O. Mariager, M. Chollet, H. T. Lemke, J. S. Robinson, J. M. Glowinski, M. P. Minitti, A. Frano, M. Fechner, N. A. Spaldin, T. Loew, B. Keimer, A. Georges, and A. Cavalleri, *Nature* **516**, 71 (2014).
- [35] M. Mitrano, A. Cantaluppi, D. Nicoletti, S. Kaiser, A. Perucchi, S. Lupi, P. Di Pietro, D. Pontiroli, M. Riccò, S. R. Clark, D. Jaksch, and A. Cavalleri, *Nature* **530**, 461 (2016).
- [36] J. W. McIver, B. Schulte, F. U. Stein, T. Matsuyama, G. Jotzu, G. Meier, and A. Cavalleri, *Nature Physics* **16**, 38 (2020).
- [37] I. Vaskivskiy, J. Gospodaric, S. Brazovskii, D. Svetin, P. Sutar, E. Goresnik, I. A. Mihailovic, T. Mertelj, and D. Mihailovic, *Science Advances* **1** (2015).
- [38] J. Zhang, X. Tan, M. Liu, S. W. Teitelbaum, K. W. Post, F. Jin, K. A. Nelson, D. N. Basov, W. Wu, and R. D. Averitt, *Nature Materials* **15**, 956 (2016).
- [39] S. W. Teitelbaum, B. K. Ofori-Okai, Y.-H. Cheng, J. Zhang, F. Jin, W. Wu, R. D. Averitt, and K. A. Nelson, “Dynamics of a persistent insulator-to-metal transition in strained manganite films,” (2019), arXiv:1906.10334 [cond-mat.str-el].
- [40] T. F. Nova, A. S. Disa, M. Fechner, and A. Cavalleri, *Science* **364**, 1075 (2019).
- [41] J. F. Dillon and C. E. Olson, *Journal of Applied Physics* **36**, 1259 (1965).
- [42] M. A. McGuire, H. Dixit, V. R. Cooper, and B. C. Sales, *Chemistry of Materials* **27**, 612 (2015).
- [43] N. D. Mermin and H. Wagner, *Phys. Rev. Lett.* **17**, 1133 (1966).
- [44] B. Huang, G. Clark, E. Navarro-Moratalla, D. R. Klein, R. Cheng, K. L. Seyler, D. Zhong, E. Schmidgall, M. A. McGuire, D. H. Cobden, W. Yao, D. Xiao, P. Jarillo-Herrero, and X. Xu, *Nature* **546**, 270 (2017).
- [45] L. Chen, J.-H. Chung, B. Gao, T. Chen, M. B. Stone, A. I. Kolesnikov, Q. Huang, and P. Dai, *Phys. Rev. X* **8**, 041028 (2018).
- [46] I. Lee, F. G. Utermohlen, D. Weber, K. Hwang, C. Zhang, J. van Tol, J. E. Goldberger, N. Trivedi, and P. C. Hammel, *Phys. Rev. Lett.* **124**, 017201 (2020).
- [47] J. L. Lado and J. Fernández-Rossier, *2D Materials* **4**, 035002 (2017).
- [48] Z. Wang, I. Gutiérrez-Lezama, N. Ubrig, M. Kroner, M. Gibertini, T. Taniguchi, K. Watanabe, A. Imamoglu, E. Giannini, and A. F. Morpurgo, *Nature Communications* **9**, 2516 (2018).
- [49] T. Song, X. Cai, M. W.-Y. Tu, X. Zhang, B. Huang, N. P. Wilson, K. L. Seyler, L. Zhu, T. Taniguchi, K. Watanabe, M. A. McGuire, D. H. Cobden, D. Xiao, W. Yao, and X. Xu, *Science* **360**, 1214 (2018).
- [50] K. L. Seyler, D. Zhong, D. R. Klein, S. Gao, X. Zhang, B. Huang, E. Navarro-Moratalla, L. Yang, D. H. Cobden, M. A. McGuire, W. Yao, D. Xiao, P. Jarillo-Herrero, and X. Xu, *Nature Physics* **14**, 277 (2018).
- [51] D. R. Klein, D. MacNeill, J. L. Lado, D. Soriano, E. Navarro-Moratalla, K. Watanabe, T. Taniguchi, S. Manni, P. Canfield, J. Fernández-Rossier, and P. Jarillo-Herrero, *Science* **360**, 1218 (2018).
- [52] Z. Sun, Y. Yi, T. Song, G. Clark, B. Huang, Y. Shan, S. Wu, D. Huang, C. Gao, Z. Chen, M. McGuire, T. Cao, D. Xiao, W.-T. Liu, W. Yao, X. Xu, and S. Wu, *Nature* **572**, 497 (2019).
- [53] L. Thiel, Z. Wang, M. A. Tschudin, D. Rohner, I. Gutiérrez-Lezama, N. Ubrig, M. Gibertini, E. Giannini, A. F. Morpurgo, and P. Maletinsky, *Science* **364**, 973 (2019).
- [54] N. Ubrig, Z. Wang, J. Teyssier, T. Taniguchi, K. Watanabe, E. Giannini, A. F. Morpurgo, and M. Gibertini, *2D Materials* **7**, 015007 (2020).
- [55] B. Huang, G. Clark, D. R. Klein, D. MacNeill, E. Navarro-Moratalla, K. L. Seyler, N. Wilson, M. A. McGuire, D. H. Cobden, D. Xiao, W. Yao, P. Jarillo-Herrero, and X. Xu, *Nature Nanotechnology* **13**, 544 (2018).
- [56] T. Song, Z. Fei, M. Yankowitz, Z. Lin, Q. Jiang, K. Hwangbo, Q. Zhang, B. Sun, T. Taniguchi, K. Watanabe, M. A. McGuire, D. Graf, T. Cao, J.-H. Chu, D. H. Cobden, C. R. Dean, D. Xiao, and X. Xu, *Nature Materials* **18**, 1298 (2019).
- [57] N. Sivadas, S. Okamoto, X. Xu, C. J. Fennie, and D. Xiao, arXiv:1808.06559 (2018).
- [58] S. W. Jang, M. Y. Jeong, H. Yoon, S. Ryee, and M. J. Han, *Phys. Rev. Materials* **3**, 031001 (2019).
- [59] D. Soriano, C. Cardoso, and J. Fernandez-Rossier, *Solid State Communications* **299**, 113662 (2019).
- [60] D. Soriano and M. I. Katsnelson, *Phys. Rev. B* **101**, 041402 (2020).
- [61] K. Momma and F. Izumi, *Journal of Applied Crystallography* **44**, 1272 (2011).
- [62] P. Jiang, C. Wang, D. Chen, Z. Zhong, Z. Yuan, Z.-Y. Lu, and W. Ji, *Phys. Rev. B* **99**, 144401 (2019).
- [63] See supplemental information.
- [64] E. Kroumova, M. Aroyo, J. Perez-Mato, A. Kirov,

- C. Capillas, S. Ivantchev, and H. Wondratschek, Phase Transitions **76**, 155 (2003).
- [65] M. S. Dresselhaus, G. Dresselhaus, and A. Jorio, *Group theory: Application to the Physics of Condensed Matter* (Springer-Verlag Berlin Heidelberg, 2008).
- [66] W. Hergert and M. R. Geilhufe, *Group theory in solid state physics and photonics: problem solving with Mathematica* (Wiley-VCH, Weinheim, 2018).
- [67] P. Giannozzi, S. Baroni, N. Bonini, M. Calandra, R. Car, C. Cavazzoni, D. Ceresoli, G. L. Chiarotti, M. Cococcioni, I. Dabo, A. D. Corso, S. de Gironcoli, S. Fabris, G. Fratesi, R. Gebauer, U. Gerstmann, C. Gougoussis, A. Kokalj, M. Lazzeri, L. Martin-Samos, N. Marzari, F. Mauri, R. Mazzarello, S. Paolini, A. Pasquarello, L. Paulatto, C. Sbraccia, S. Scandolo, G. Sclauzero, A. P. Seitsonen, A. Smogunov, P. Umari, and R. M. Wentzcovitch, Journal of Physics: Condensed Matter **21**, 395502 (2009).
- [68] P. Giannozzi, O. Andreussi, T. Brumme, O. Bunau, M. B. Nardelli, M. Calandra, R. Car, C. Cavazzoni, D. Ceresoli, M. Cococcioni, N. Colonna, I. Carnimeo, A. D. Corso, S. de Gironcoli, P. Delugas, R. A. DiStasio, A. Ferretti, A. Floris, G. Fratesi, G. Fugallo, R. Gebauer, U. Gerstmann, F. Giustino, T. Gorni, J. Jia, M. Kawamura, H.-Y. Ko, A. Kokalj, E. Kçkbenli, M. Lazzeri, M. Marsili, N. Marzari, F. Mauri, N. L. Nguyen, H.-V. Nguyen, A. O. de-la Roza, L. Paulatto, S. Ponce, D. Rocca, R. Sabatini, B. Santra, M. Schlipf, A. P. Seitsonen, A. Smogunov, I. Timrov, T. Thonhauser, P. Umari, N. Vast, X. Wu, and S. Baroni, Journal of Physics: Condensed Matter **29**, 465901 (2017).
- [69] G. Kresse and J. Furthmller, Computational Materials Science **6** (1996).
- [70] G. Kresse and J. Furthmller, Phys. Rev. B **54**, 11169 (1996).
- [71] S. Baroni, S. de Gironcoli, A. Dal Corso, and P. Giannozzi, Rev. Mod. Phys. **73**, 515 (2001).
- [72] M. Frst, C. Manzoni, S. Kaiser, Y. Tomioka, Y. Tokura, R. Merlin, and A. Cavalleri, Nature Physics **7**, 854 (2011).
- [73] X. Gonze and C. Lee, Phys. Rev. B **55**, 10355 (1997).
- [74] R. F. Wallis and A. A. Maradudin, Phys. Rev. B **3**, 2063 (1971).
- [75] R. Mankowsky, M. Frst, T. Loew, J. Porras, B. Keimer, and A. Cavalleri, Phys. Rev. B **91**, 094308 (2015).
- [76] A. Sell, A. Leitenstorfer, and R. Huber, Opt. Lett. **33**, 2767 (2008).
- [77] T. Kampfath, K. Tanaka, and K. A. Nelson, Nature Photonics **7**, 680 (2013).
- [78] A. Kitaev, Annals of Physics **321**, 2 (2006), january Special Issue.
- [79] J. G. Rau, E. K.-H. Lee, and H.-Y. Kee, Phys. Rev. Lett. **112**, 077204 (2014).
- [80] P. A. McClarty, X.-Y. Dong, M. Gohlke, J. G. Rau, F. Pollmann, R. Moessner, and K. Penc, Phys. Rev. B **98**, 060404 (2018).
- [81] G. L. Stamokostas, P. E. Lapas, and G. A. Fiete, Phys. Rev. B **95**, 064410 (2017).
- [82] M. Hoffmann, A. Ernst, W. Hergert, V. N. Antonov, W. A. Adeagbo, R. Matthias Geilhufe, and H. Ben Hamed, physica status solidi (b) **n/a**, 10.1002/pssb.201900671.
- [83] E. Granado, A. Garca, J. A. Sanjurjo, C. Rettori, I. Torriani, F. Prado, R. D. Snchez, A. Caneiro, and S. B. Oseroff, Phys. Rev. B **60**, 11879 (1999).
- [84] R. M. Geilhufe and W. Hergert, Frontiers in Physics **6**, 86 (2018).
- [85] H. T. Stokes, D. M. Hatch, and B. J. Campbell, “Isodisort, isotropy software suite, iso.byu.edu,”.
- [86] D. T. Larson and E. Kaxiras, Phys. Rev. B **98**, 085406 (2018).

SUPPLEMENTAL MATERIAL FOR “PHONON-MEDIATED DIMENSIONAL CROSSOVER IN BILAYER CrI₃”

In this supplemental material, we discuss additional group theory aspects of bilayer and monolayer CrI₃. Also, we describe in detail the phonon frequency and the non-linear phonon couplings first principles calculations.

Γ -POINT PHONON FREQUENCIES AND MACROSCOPIC DIELECTRIC TENSOR

In this section we list all the phonon frequencies at the Γ point, the macroscopic dielectric tensor, and the Born charges. We use five different approaches, which show a good agreement among all of them. Table [III] shows converged phonon frequencies at the Γ point of the CrI₃ bilayer with the C2/m space group. The different approaches we employ are described below:

qe1: QUANTUM ESPRESSO [67, 68] calculation using Density Functional Perturbation Theory (dfpt). GGA-PAW potentials were employed with Ecut=55 Ry and Ecutrho=490 Ry. k-grid sampling of 12x12x1 and Van der Waals correction of type grimme-d2 were used.

qe2: same as qe1, imposing the acoustic sum rule to the dynamical matrix, $\sum_{\mathbf{L},j} C_{\alpha i, \beta j}(\mathbf{R}_{\mathbf{L}}) = 0$. Corrects the non analytic contribution to LO $\omega_L = \sqrt{\omega_o^2 + 4\pi^2 Z^{*2} / \Omega \epsilon_{\infty} M}$ are also included.

vasp3: VASP[69, 70] calculation using finite differences (fd) (IBRION=6, NFREE=4). GGA-PAW potentials were employed with ENCUT=600eV. k-grid sampling of 12x12x1 and Van der Waals correction of type grimme-d2 were used.

vasp4: VASP calculation using finite differences (IBRION=6 NFREE=4). LDA-PAW potentials were employed with ENCUT=600eV. k-grid sampling of 12x12x1 and NO VdW correction.

vasp5: VASP calculation using DFPT (IBRION=8). LDA-PAW potentials were employed with ENCUT=600eV. k-grid sampling of 12x12x1 and NO VdW correction.

3.86908	0.000000	-0.004342
0.000000	3.869087	0.000000
-0.004340	0.000000	1.490740

TABLE I. Macroscopic dielectric tensor in cartesian coordinates as obtained with QE and DFPT.

4.009906	0.000000	-0.005896
0.000000	4.011021	0.000000
-0.005896	0.000000	1.491395

TABLE II. Macroscopic dielectric tensor in cartesian coordinates as obtained with VASP and DFPT.

Born effective charges

The effective charge tensors $Z_{\kappa,ij}^*$ (units of the electron electric charge e and in cartesian axis) of atom κ are listed below. The Born effective charge is defined as [71, 73]

$$Z_{\alpha,i}^* = \sum_{\kappa,j} Z_{\kappa,ij}^* \frac{e_{\alpha,\kappa,j}}{\sqrt{m_{\kappa}}}, \quad (4)$$

where α labels the phonon mode, i the direction in cartesian coordinates, κ labels the atoms in the unit cell, m_{κ} is the mass of atoms κ , and $e_{\alpha,\kappa,j}$ corresponds to the dynamical matrix eigenvector α , atom κ , in the direction j normalized as $\sum_{\kappa,j} (e_{\alpha,\kappa,j})^* e_{\beta,\kappa,j} = \delta_{\alpha\beta}$.

atom 1 Cr			atom 9 I		
2.50670	0.01211	0.0035	0.06017	0.09685	-0.10598
0.01266	2.48423	-0.00869	-0.41963	-0.59530	-0.46809
-0.00018	-0.00217	0.27999	0.06017	-0.09685	-0.10598
atom 2 Cr			atom 10 I		
2.50670	-0.01211	0.00352	-1.10547	0.43882	0.27730
-0.01266	2.48423	0.00869	0.43112	-0.55676	0.44096
-0.00018	0.00217	0.27999	0.05116	0.08974	-0.0775
atom 3 Cr			atom 11 I		
2.50670	-0.01211	0.00352	-0.37557	0.00000	-0.55006
-0.01266	2.48423	0.00869	0.00000	-1.32030	0.00000
-0.00018	0.00218	0.28094	-0.11557	0.00000	-0.10817
atom 4 Cr			atom 12 I		
2.50670	0.01211	0.00352	-0.31861	0.00000	-0.55899
0.01266	2.48423	-0.00869	0.00000	-1.37494	0.00000
-0.00018	-0.00218	0.28094	-0.10654	0.00000	-0.11383
atom 5 I			atom 13 I		
-0.31877	0.00000	-0.55912	-1.06967	-0.41268	0.27350
0.00000	-1.37542	0.00000	-0.41970	-0.59544	-0.46806
-0.10597	0.00000	-0.11291	0.05985	-0.09629	-0.10442
atom 6 I			atom 14 I		
-0.37544	0.00000	-0.55003	-1.10520	0.43869	0.27732
0.00000	-1.32046	0.00000	0.43116	-0.55665	0.44089
-0.11621	0.00000	-0.1097	0.05145	0.09024	-0.07844
atom 7 I			atom 15 I		
-1.10547	-0.43882	0.27730	-1.10520	-0.43869	0.27732
-0.43112	-0.55676	-0.44096	-0.43116	-0.55665	-0.44089
0.05116	-0.08974	-0.07759	0.05145	-0.09024	-0.07844
atom 8 I			atom 16 I		
-1.06968	0.41271	0.27359	-1.06967	0.41268	0.27350
0.41963	-0.59530	0.46809	0.41970	-0.59544	0.46806
0.06017	0.09685	-0.10598	0.05985	0.09629	-0.10442

TABLE IV. Effective charge tensors $Z_{\kappa,ij}^*$ (units of the electron electric charge e and in cartesian axis) for each atom κ in the unit cell obtained with the **qe1** method.

#	GGA + VdW			LDA			#	GGA + VdW			LDA		
	qe1 dfpt	qe2 dfpt	vasp3 fd	vasp4 fd	vasp5 dfpt	qe1 dfpt		qe2 dfpt	vasp3 fd	vasp4 fd	vasp5 dfpt		
4	0.2385	0.4976	0.4604	0.3783	C	27	3.2697	3.2740	3.2433	3.2673	3.2269		
5	0.3690	0.4989	0.4670	0.3864	0.1714	28	3.2807	3.2937	3.2450	3.2891	3.2303		
6	0.4477	0.9079	0.9595	0.7972	0.9079	29	3.4095	3.4022	3.3609	3.4638	3.4018		
7	1.6958	1.7132	1.6860	1.5308	1.4793	30	3.4183	3.4218	3.3665	3.4722	3.4203		
8	1.7237	1.7377	1.7040	1.5371	1.5042	31	3.4452	3.4397	3.3920	3.4741	3.4293		
9	1.7367	1.7564	1.7141	1.5562	1.5239	32	3.4454	3.4485	3.3983	3.4783	3.4310		
10	1.7413	1.7628	1.7288	1.5587	1.5372	33	3.8140	3.8112	3.7515	3.9069	3.9070		
11	2.0703	2.1097	2.0503	1.7126	1.6859	34	3.9230	3.9243	3.8707	3.9697	3.9532		
12	2.0853	2.1280	2.0574	1.7243	1.6976	35	4.0210	4.0156	3.9941	4.0491	4.0344		
13	2.5990	2.6087	2.5759	2.2839	2.2798	36	4.0290	4.0221	3.9950	4.0494	4.0366		
14	2.6116	2.6247	2.5833	2.3164	2.3034	37	5.5624	5.9087	5.8083	6.5331	6.5479		
15	2.6443	2.6620	2.6371	2.4387	2.3883	38	5.6466	6.0482	5.8098	6.5354	6.5505		
16	2.6632	2.6722	2.6418	2.4546	2.4212	39	6.0618	6.1663	6.0943	6.8176	6.8098		
17	2.6633	2.6754	2.6473	2.4709	2.4273	40	6.1175	6.1734	6.1014	6.8193	6.8138		
18	2.7513	2.7614	2.7048	2.4725	2.4423	41	6.1473	6.1793	6.1042	6.8248	6.8228		
19	2.7664	2.9146	2.8981	2.6894	2.7276	42	6.1858	6.2221	6.1201	6.8332	6.8248		
20	2.8047	2.9525	2.9078	2.6906	2.7291	43	6.5188	6.5480	6.4940	7.2969	7.2970		
21	3.0059	3.0036	2.9605	3.0827	3.0360	44	6.5201	6.5638	6.5038	7.3029	7.3030		
22	3.0340	3.0339	2.9907	3.0894	3.0445	45	6.5378	6.6344	6.5193	7.3076	7.3071		
23	3.0363	3.0376	3.0041	3.0988	3.0666	46	6.6435	6.6723	6.5230	7.3136	7.3132		
24	3.0384	3.0417	3.0092	3.1003	3.0679	47	7.0222	7.3521	7.2560	7.9413	7.9799		
25	3.2498	3.2580	3.2352	3.2557	3.1649	48	7.0914	7.4011	7.2676	7.9484	7.9914		
26	3.2694	3.2730	3.2365	3.2628	3.2023								

TABLE III. Γ -point phonon frequencies for bilayer CrI_3 with space group $C2/m$. The method abbreviations are: qe = Quantum-Espresso, dfpt= Density Functional Perturbation Theory, fd= Finite difference

atom 1 Cr			atom 9 I		
2.47034	0.00975	0.00028	-1.05146	-0.41069	0.28647
0.01476	2.45196	-0.01247	-0.42081	-0.57647	-0.48663
-0.00207	-0.00222	0.27215	0.05816	-0.09177	-0.09762
atom 2 Cr			atom 10 I		
2.47034	-0.00975	0.00028	-1.08708	0.43826	0.28929
-0.01475	2.45262	0.01258	0.43034	-0.53772	0.45867
-0.00207	0.00222	0.27215	0.05298	0.09212	-0.07155
atom 3 Cr			atom 11 I		
2.47028	-0.00955	0.00023	-0.36021	0.00000	-0.57005
-0.01476	2.45196	0.01247	-0.00050	-1.30942	-0.00044
-0.00169	0.00193	0.27170	-0.11277	0.00000	-0.10142
atom 4 Cr			atom 12 I		
2.47028	0.00955	0.00023	-0.30334	0.00000	-0.58193
0.01475	2.45262	-0.01258	0.00061	-1.36813	0.00051
-0.00169	-0.00193	0.27170	-0.10721	0.00000	-0.10519
atom 5 I			atom 13 I		
-0.30351	0.00000	-0.58214	-1.05127	-0.41066	0.28650
-0.00061	-1.36813	-0.00051	-0.42068	-0.57582	-0.48662
-0.10894	0.00000	-0.10684	0.05856	-0.09302	-0.09877
atom 6 I			atom 14 I		
-0.36020	0.00000	-0.56990	-1.08718	0.43838	0.28924
0.00050	-1.30942	0.00044	0.43028	-0.53701	0.45876
-0.10946	0.00000	-0.10026	0.05325	0.09106	-0.06906
atom 7 I			atom 15 I		
-1.08708	-0.43826	0.28929	-1.08718	-0.43838	0.28924
-0.43028	-0.53701	-0.45876	-0.43034	-0.53772	-0.45867
0.05298	-0.09212	-0.07155	0.05325	-0.09106	-0.06906
atom 8 I			atom 16 I		
-1.05146	0.41069	0.28647	-1.05127	0.41066	0.28650
0.42068	-0.57582	0.48662	0.42081	-0.57647	0.48663
0.05816	0.09177	-0.09762	0.05856	0.09302	-0.09877

TABLE V. Effective charge tensors $Z_{\kappa,ij}^*$ (units of the electron electric charge e and in cartesian axis) for each atom κ in the unit cell obtained with the **vasp3** method.

NON-LINEAR COEFFICIENTS

In this section, we calculate the non-linear coefficients for the energy potential

$$\begin{aligned}
V[Q_{\text{IR}}, Q_{\text{R}(i)}] &= \frac{1}{2} \Omega_{\text{IR}}^2 Q_{\text{IR}}^2 + \sum_{i=1}^2 \frac{1}{2} \Omega_{\text{R}(i)}^2 Q_{\text{R}(i)}^2 \\
&+ \sum_{i=1}^2 \frac{\beta_i}{3} Q_{\text{R}(i)}^3 + Q_{\text{IR}}^2 \sum_{i=1}^2 \gamma_i Q_{\text{R}(i)} + \delta Q_{\text{R}(1)}^2 Q_{\text{R}(2)} \\
&+ \epsilon Q_{\text{R}(1)} Q_{\text{R}(2)}^2 + Q_{\text{R}(3)}^2 \sum_{i=1}^2 \zeta_i Q_{\text{R}(i)}. \quad (5)
\end{aligned}$$

shown in the main text and repeated here for reference. To determine these coefficients, we follow the procedure described in Ref.[4]. The displacement of atom κ in the unit cell, direction j , in terms of the normal mode amplitude Q_α , is given by

$$u_{\alpha,\kappa,j} = \frac{Q_\alpha}{\sqrt{m_\kappa}} e_{\alpha,\kappa,j}, \quad (6)$$

where m_κ is the mass of atom κ , and $e_{\alpha,\kappa,j}$ is a dynamical matrix eigenvectors normalized as $\sum_{\kappa,j} (e_{\alpha,\kappa,j})^* e_{\beta,\kappa,j} = \delta_{\alpha\beta}$. The coefficients are listed in Table VI.

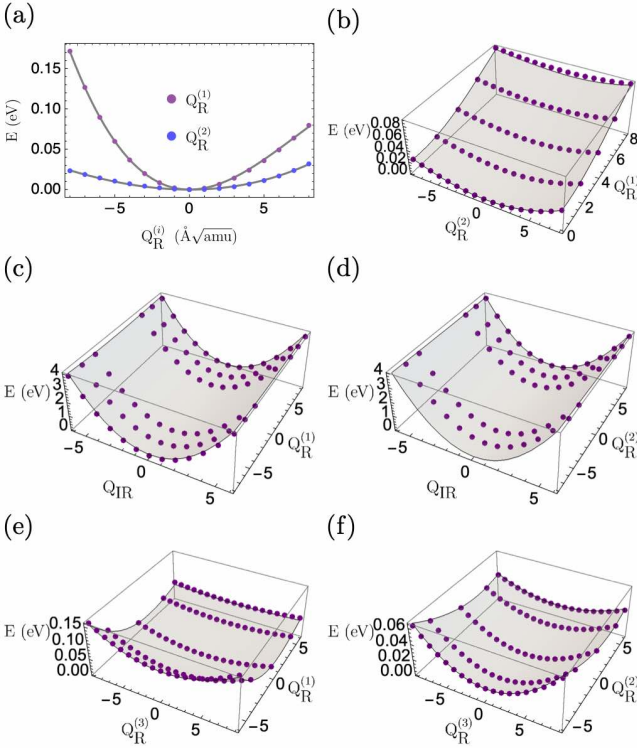


FIG. 5. (Color online) Total energy as a function of the phonon mode amplitudes. In each panel, we vary the indicated phonon amplitudes to obtain the energy surface, keeping the other modes at equilibrium. From fitting to these curves, we can extract all the coefficients appearing in the non-linear potential Eq. (5).

Coefficient	Value	Units
$\Omega_R^{(1)2}$	3.766×10^{-3}	$\text{eV}/(\text{\AA}\sqrt{\text{amu}})^2$
$\Omega_R^{(2)2}$	8.64113×10^{-4}	$\text{eV}/(\text{\AA}\sqrt{\text{amu}})^2$
$\Omega_R^{(3)2}$	8.82608×10^{-4}	$\text{eV}/(\text{\AA}\sqrt{\text{amu}})^2$
β_1	-2.72×10^{-4}	$\text{eV}/(\text{\AA}\sqrt{\text{amu}})^3$
β_2	2.22×10^{-5}	$\text{eV}/(\text{\AA}\sqrt{\text{amu}})^3$
$\gamma_1(47)$	2.32×10^{-4}	$\text{eV}/(\text{\AA}\sqrt{\text{amu}})^3$
$\gamma_2(47)$	-1.89×10^{-4}	$\text{eV}/(\text{\AA}\sqrt{\text{amu}})^3$
$\gamma_1(41)$	-1.82×10^{-4}	$\text{eV}/(\text{\AA}\sqrt{\text{amu}})^3$
$\gamma_2(41)$	-6.33×10^{-5}	$\text{eV}/(\text{\AA}\sqrt{\text{amu}})^3$
δ	-7.79×10^{-6}	$\text{eV}/(\text{\AA}\sqrt{\text{amu}})^3$
ϵ	-3.06×10^{-5}	$\text{eV}/(\text{\AA}\sqrt{\text{amu}})^3$
ζ_1	-6.19×10^{-5}	$\text{eV}/(\text{\AA}\sqrt{\text{amu}})^3$
ζ_2	-3.07×10^{-5}	$\text{eV}/(\text{\AA}\sqrt{\text{amu}})^3$

TABLE VI. Non-linear coefficients obtained by fitting the energy surfaces shown in Fig. 5. The frequencies $\Omega_R^{(i)}$ are in good agreement with dynamical matrix diagonalization results. The coefficients $\gamma_i(47)$ are relevant for a laser incident in the z -direction, while the coefficients $\gamma_i(41)$ are relevant a pulse incident in the y -direction.

MONOLAYER CrI_3 GROUP THEORY ANALYSIS

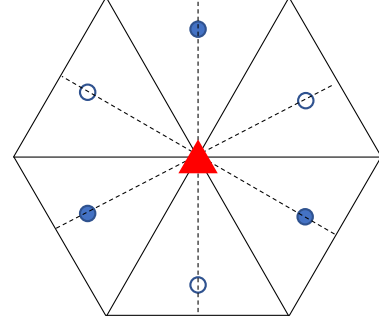


FIG. 6. (Color online) Symmetry operations on a CrI_3 unit cell. Cr atoms sit at the corners of the hexagon, while the blue circles represent the I atoms located out-of-plane. Filled atoms are below the plane and empty circles are above the plane. The red triangle at the center of the hexagon represents C_3 rotation. Solid lines joining the vertices represent C_2 rotation axis, and dotted lines correspond to reflection planes σ_d . Additionally, we find that $S_6 = \sigma_h C_6$ and inversion i are also symmetries of the lattice.

Now we perform a group theory analysis on monolayer and bilayer CrI_3 . Our goal is to determine the properties of the Γ point phonons such as irreducible representations, lattice displacements, Raman and infrared activity and non-linear phonon coupling. For this, we employ GTPack [66, 84], ISOTROPY [85], and the Bilbao Crystallographic Server [64].

Infrared and Raman active modes

Ab-initio studies of the Raman spectrum on monolayer CrI_3 have postulated that the space group is $R\bar{3}2m$ (No. 166) [86]. However, more recent Raman experiments have identified the structure to belong to the $p\bar{3}1m$ (D_{3d}^1) double space group.

In Fig. (6) we show a diagram with the point group operations we identified in the lattice shown in monolayer CrI_3 . The point group is found to be D_{3d} . The character table for the point group D_{3d} is shown in panel (b) [65]. We start determining the infrared and Raman active modes in this system. For this, we first calculate the equivalence representation Γ^{equiv} keeping in mind that there are 8 atoms per unit cell, two Cr atoms and six I atoms. Γ^{equiv} is given in Table VII.

	E	C_3	C_2	i	S_6	σ_d
Γ^{equiv}	8	2	2	0	0	2

TABLE VII. Equivalence representation.

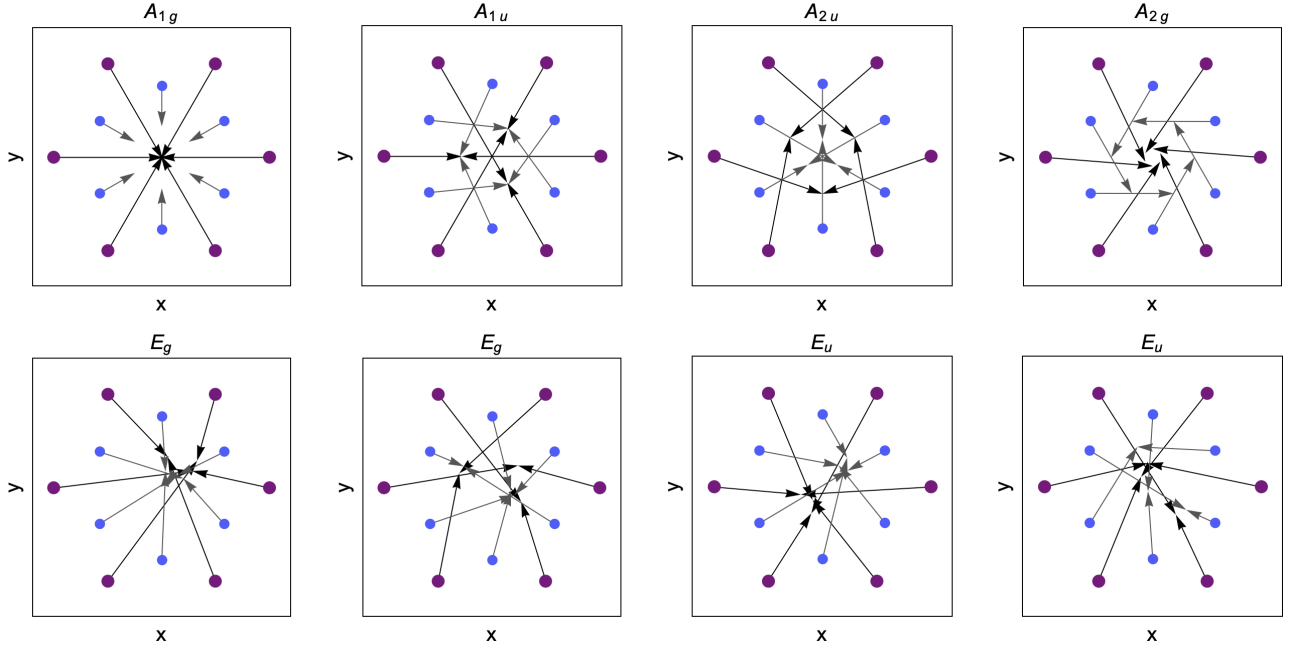


FIG. 7. (Color online) CrI_3 vibration modes projected onto the xy -plane for clarity. The one-dimensional representations (A_j) have one partner. The modes of the two-dimensional representations E_j have two partners each.

Using the decomposition theorem [65] we find

$$\Gamma^{equiv} = 2A_{1g} \oplus E_g \oplus A_{1u} \oplus A_{2u} \oplus E_u. \quad (7)$$

In this point group, the representation of the vector is $\Gamma_{vec} = E_u \oplus A_{2u}$. Then, the representation of the lattice vibrations is

$$\begin{aligned} \Gamma_{latt.vib.} &= \Gamma^{equiv} \otimes \Gamma_{vec} \\ &= 2A_{1g} \oplus 2A_{2g} \oplus 4E_g \oplus A_{1u} \oplus 3A_{2u} \oplus 4E_u. \end{aligned} \quad (8)$$

From the character table, we can conclude that monolayer CrI_3 has six Raman active modes with representations A_{1g} , and E_g . Two frequencies are non-degenerate and four are doubly-degenerate. The two A_{1g} modes correspond to “breathing” modes, where the lattice expands and contracts preserving all the symmetries. One of them is in-plane and the other one is out-of-plane. Modes that

D_{3d}	E	$2C_3$	$3C_2$	i	$2S_6$	$3\sigma_d$		
A_{1g}	1	1	1	1	1	1		$x^2 + y^2, z^2$
A_{2g}	1	1	-1	1	1	-1	I_z	
E_g	2	-1	0	2	-1	0	(I_x, I_y)	$(x^2 - y^2, xy), (yz, zx)$
A_{1u}	1	1	1	-1	-1	-1		
A_{2u}	1	1	-1	-1	-1	1		z
E_u	2	-1	0	-2	1	0		(x, y)

TABLE VIII. D_{3d} point group character table.

transform as A_{2u} , and E_u are infrared active. This results can be corroborated with the Bilbao Crystallography Server. The vibration eigenvectors for a given representation Γ can be obtained using projection operators $P^{(\Gamma)}$ in the displacement representation as [65]

$$Q^\Gamma = P^{(\Gamma)} \otimes \zeta, \quad (9)$$

where $\zeta = x_1, y_1, z_1, \dots, x_N, y_N, z_N$ is an arbitrary vector of dimension $3N$, and N is the number of atoms in the unit cell. Fig. 7 shows the monolayer CrI_3 vibrational modes, projected onto the xy -plane for clarity.

BILAYER CHROMIUM TRIIODIDE GROUP THEORY ASPECTS.

In this section, we show explicitly the character table for the relevant point group, and the transformation from the conventional to the primitive unit cell.

The transformation is given by

$$\mathcal{T} = \begin{pmatrix} 1/2 & 1/2 & 0 \\ -1/2 & 1/2 & 0 \\ 0 & 0 & 1 \end{pmatrix} + \begin{pmatrix} 1/2 \\ 1/2 \\ 0 \end{pmatrix}. \quad (10)$$

The character table for the point group C_{2h} is

C_{2h}	E	C_2	i	σ_h		
A_g	1	1	1	1	I_z	x^2, y^2, z^2, xy
B_g	1	-1	1	-1	I_x, I_y	xz, yz
A_u	1	1	-1	-1	z	
B_u	1	-1	-1	1	x, y	

TABLE IX. C_{2h} point group character table [65].